RSC Advances

PAPER

Cite this: *RSC Adv.*, 2022, **12**, 29170

3D hierarchical cobalt vanadate nanosheet arrays on Ni foam coupled with redox additive for enhanced supercapacitor performance†

Van Thanh Nguyen, [a] Fitri Nur Indah Sari[a] and Jyh-Ming Ting *[ab]

Received 9th September 2022
Accepted 4th October 2022

DOI: 10.1039/d2ra05679h

rsc.li/rsc-advances

Room-temperature synthesized 3D hierarchical cobalt vanadate ($Co_3V_2O_8$) nanosheet arrays on Ni foam for use as supercapacitor electrode is presented. In a 3 M KOH electrolyte, the electrode exhibits a capacitance of 109.9 mA h g^{-1} (878.9 F g^{-1}) at a current density of 1 A g^{-1}. The capacitance is enhanced to 198.1 mA h g^{-1} (1584.5 F g^{-1}) at 1 A g^{-1} through the addition of 0.05 M redox-additive $K_3[Fe(CN)_6]$ into the KOH electrolyte. Furthermore, the $Co_3V_2O_8$/activated carbon asymmetric supercapacitor cell with the advanced electrolyte outperforms most reported $Co_3V_2O_8$-based electrodes with a remarkable energy density of 55.5 W h kg^{-1} at an 800 W kg^{-1} power density. Combining a facile synthetic strategy and excellent electrochemical performance, the obtained $Co_3V_2O_8$ exhibits potential for practical application.

1. Introduction

Exploration of renewable energy has been a continuous effort for reaching a green and sustainable world.[1,2] One of the keys is related to an advanced energy storage device, namely, asymmetric supercapacitors (ASCs). ASC is composed of a positive electrode made from a faradaic, battery-like material and a negative electrode made from a non-faradaic, electric double-layer material.[2–4] To date, the most effective negative electrodes are carbon-based materials.[5–7] Thus, recent research interest in ASCs focuses on positive electrode materials.[8–11] One of the battery-like electrode materials, *i.e.*, metal vanadate, holds great potential owing to its layered structure and rich valence states. Common metal vanadates include $Ni_{1-x}V_xO_2$, $Zn_2V_2O_7$, $BiVO_4$, $Ni_3V_2O_8$, and $Co_3V_2O_8$.[12–15] Among them, cobalt vanadate ($Co_3V_2O_8$) has drawn significant attention owing to its excellent stability, outstanding capacitance, low-toxicity, and simplicity of preparation.

Hydrothermally synthesized $Co_3V_2O_8$ has a specific capacitance (C_{sp}) of 505 F g^{-1} at 0.625 A g^{-1} and an energy density (E_d) of 28 W h kg^{-1} at a power density (P_d) of 1400 W kg^{-1}.[16] One-pot solvothermal $Co_3V_2O_8$/graphene composite showed a C_{sp} of 528.2 F g^{-1} at 0.5 A g^{-1}, and 80% capacitance remaining after 5000 cycles.[13] Hydrothermally synthesized $Co_3V_2O_8$ nanoplate electrode shows a remarkable C_{sp} of 739 F g^{-1} at 0.5 A g^{-1} and 2000 cycles retention of 95.3%.[17] Electrode based on 3D porous $Co_3V_2O_8$ microflowers synthesized using a co-precipitation method exhibits a C_{sp} of 351 F g^{-1} at 1 A g^{-1} with 103% capacitance retention after 30 000 cycles.[18] An E_d of 19 W h kg^{-1} at P_d of 375.8 W kg^{-1} was also reported. NiO–$Co_3(VO_4)_2$ grown on nickel foam shows a C_{sp} of 1166 F g^{-1} at 0.5 A g^{-1} and cycle stability of 99.4% after 5000 cycles.[19] The E_d is 38.8 W h kg^{-1} at a P_d of 397.9 W kg^{-1}. Heterostructure of $Co_3V_2O_8$–$Ni_3V_2O_8$/carbon composite exhibits C_{sp} of 1731 F g^{-1} at 1 A g^{-1} and an E_d of 59.7 W h kg^{-1} at high P_d of 1970 W kg^{-1}.[20] The excellent SC performance is obtained due to the rich redox activities of the cobalt vanadate, and high active surface areas. On the other hand, the use of redox additive (RA) electrolyte has also been demonstrated to enhance the C_{sp}.[21–25]

Herein, we present a room-temperature process to synthesize $Co_3V_2O_8$ nanowalls on Ni foam (NF) using a template-assisted growth. Also, $K_3[Fe(CN)_6]$ RA electrolyte is used to enhance ionic conductivity of electrolyte and provide additional redox reactions, targeting in the further capacitance improvements. With the use of the RA electrolyte, a capacitance of 198.1 mA h g^{-1} (1584.5 F g^{-1}) at 1 A g^{-1} is demonstrated. Furthermore, we show that an ASC having an activated carbon (AC) negative electrode, $Co_3V_2O_8$ positive electrode, and the RA electrolyte provides an excellent E_d of 55.5 W h kg^{-1} at a P_d of 800 W kg^{-1} and 82% capacitance remaining after 10 000 cycles.

2. Experimental

2.1 Chemicals

All chemicals were used as received. 2-methylimidazole (2-MIM, 99%, Sigma Aldrich), cobalt nitrate hexahydrate ($Co(NO_3)_2 \cdot 6H_2O$, 98%, Baker Analyzed Reagent), and sodium orthovanadate (Na_3VO_4, ≥90%, Sigma Aldrich), and potassium hydroxide (KOH, ≥85%, Honeywell Fluka).

[a]*Department of Materials Science and Engineering, National Cheng Kung University, Tainan 70101, Taiwan. E-mail: jting@mail.ncku.edu.tw*

[b]*Hierarchical Green-Energy Materials (Hi-GEM) Research Center, National Cheng Kung University, Tainan 70101, Taiwan*

† Electronic supplementary information (ESI) available. See DOI: https://doi.org/10.1039/d2ra05679h

2.2 Synthesis of ZIF-67

ZIF-67 was synthesized by a precipitation method.[26] A piece of 2 × 3 cm NF was first cleaned with 10 mL HCl 37% for 5 minutes, followed by deionized (DI) water and ethanol in sequence washing. The NF is used as the substrate for the growth of ZIF-67. To grow ZIF-67, a 20 mL solution A consisting of 2 mmol $Co(NO_3)_2 \cdot 6H_2O$ was first made under stirring for 30 minutes to form solution A. Meanwhile, 20 mL solution B containing 16 mmol of 2-MIM was also prepared. After that, the two prepared solutions were quickly mixed. After 5 minutes of stirring, the washed NF was then deep into the prepared solution at room temperature for 3 hours. The final product was achieved after washing with DI water and ethanol, followed by drying with flowing nitrogen gas.

2.3 Synthesis of $Co_3V_2O_8$

To convert the ZIF-67 into $Co_3V_2O_8$, the ZIF-67@NF was immersed in 20 mL of 0.1 M Na_3VO_4 aqueous solution. After a three hours' ion exchange process at room temperature, the resulting NF was soaked in ethanol and DI water, then dried under a nitrogen flow. The active material on the NF was calculated to be 1.6 mg cm^{-2}.

2.4 Material characterizations

The morphology and structure were examined utilizing transmission electron microscopy (TEM, JEOL-2100F CS STEM) and scanning electron microscopy (SEM, JSM-6701F). X-ray photoelectron spectroscopy (XPS, PHI 5000) was used to analyze the surface chemistry. Crystalline structure was examined using X-ray diffraction (XRD, Rigaku X-ray Diffractometer) with a CuKα radiation source.

2.5 Electrochemical characterizations

Electrochemical characterization of the electrode was conducted using a three-electrode cell having 3 M KOH or RA electrolyte. The $Co_3V_2O_8$ nanowalls on NF (1 cm × 1 cm) was used as the working electrode. The reference was a saturated calomel electrode (SCE) with saturated 3 M KCl aqueous solution, and a Pt rod was the counter electrode. All of the electrochemical tests were done using an Autolab NOVA system. Electrochemical impedance spectroscopy (EIS) analysis was performed with 5 mV amplitude and 100 kHz to 0.01 Hz frequency range.

2.6 Fabrication of ASC

The ASC consists of $Co_3V_2O_8$ and AC (demoted as $Co_3V_2O_8$//AC) was assembled. As-synthesized $Co_3V_2O_8$ on NF was used as the positive electrode. For the AC negative electrode, 8 mg of AC, 1 mg of polyvinylidene fluoride, 1 mg of carbon black, and 1 mL of *N*-methyl-2-pyrrolidone were first prepared. After 12 h of stirring, the obtained slurry was dropped cast on an NF substrate, then dried at 60 °C for 12 h. The $Co_3V_2O_8$ positive electrode was directly used after the synthesis. The negative electrode's active mass was decided following the charge balance relationship, as shown in eqn (1):

$$\frac{m_+}{m_-} = \frac{C_{sp-}}{C_{sp+}} \times \frac{\Delta V_-}{\Delta V_+} \quad (1)$$

where m, ΔV, and C_{sp} are the mass, potential window, and specific capacitance, respectively; while "−" and "+" represent the negative and positive electrodes, respectively.

The C_{sp} was determined using eqn (2):

$$C_{sp} = \frac{I \times \Delta t}{m \times 3.6} \ \left(\text{mA h g}^{-1}\right) \quad (2)$$

where t is the discharge period (s), V is the potential window (V), m represents the active material's weight (g), and I the discharge current (A). E_d and P_d were determined using eqn (3) and (4), respectively:

$$E_d = \frac{1}{2} C_{sp} (\Delta V)^2 \ \left(\text{W h kg}^{-1}\right) \quad (3)$$

$$P_d = \frac{E_d}{\Delta t} \left(\text{W kg}^{-1}\right) \quad (4)$$

3. Results and discussion

$Co_3V_2O_8$ were grown on ZIF-67@NF where the ZIF-67 homogenously distributes on the NF (Fig. S1A†) with a uniform thickness of 2.2 μm (Fig. S1B†) and a plate-like morphology (Fig. S1C†). After the ion exchange process, uniform coverage of the material on the NF surface remains, as shown in Fig. 1A. The nanoplate ZIF-67 turns into nanowall morphology (Fig. 1B). The average thickness of the nanowalls is about 30 nm (Fig. 1C), much less than that of the nanoplates. The nanowall is further examined using TEM, as illustrated in Fig. 1D. A high-resolution TEM image (Fig. 1E) shows d-spacings of 0.208 and 0.254 nm, corresponding to the (042) and (112) planes of $Co_3V_2O_8$ (JCPDS no. 74-1487). Various diffraction rings in the selected area electron diffraction (SAED) pattern (Fig. 1F) are indexed to the polycrystalline $Co_3V_2O_8$, confirming the formation of $Co_3V_2O_8$ nanowalls. XRD analysis also indicates the formation of low-crystallinity $Co_3V_2O_8$ (Fig. S2†). EDS elemental distribution and mappings are shown in Fig. 1H and G, respectively. The Co, V, and O uniformly distribute throughout the nanowalls. The Co and V both exhibit multi-valence states of Co^{2+}/Co^{3+} and V^{4+}/V^{5+}, respectively, as shown by XPS analysis (Fig. S3†).

CV curves of the $Co_3V_2O_8$ electrode evaluated using the 3 M KOH and RA electrolytes are displayed in Fig.s S4A† and 2A, respectively. Fig. 2B shows the comparison of the CV curves acquired at 5 mV s^{-1}. With the use of the KOH electrolyte, there are two redox peaks couple, which are ascribed to the reversible redox reactions of Co(II) ↔ Co(III) (at ∼0.03 and ∼0.13 V) and Co(III) ↔ Co(IV) (at ∼0.25 and 0.43 V) reactions, respectively.[27] The existence of the redox peaks indicates that the $Co_3V_2O_8$ electrode is pseudocapacitive. In the case of the RA electrolyte, two redox peaks couple shifting to the positive side are seen. The couple redox peak for Co(II) ↔ Co(III) is also seen. The second redox peaks at the right are attributed to the addition of $Fe(CN)_6^{3-}/Fe(CN)_6^{4-}$ (0.5 and 0.27 V *vs.* SCE) redox peaks.[22,28]

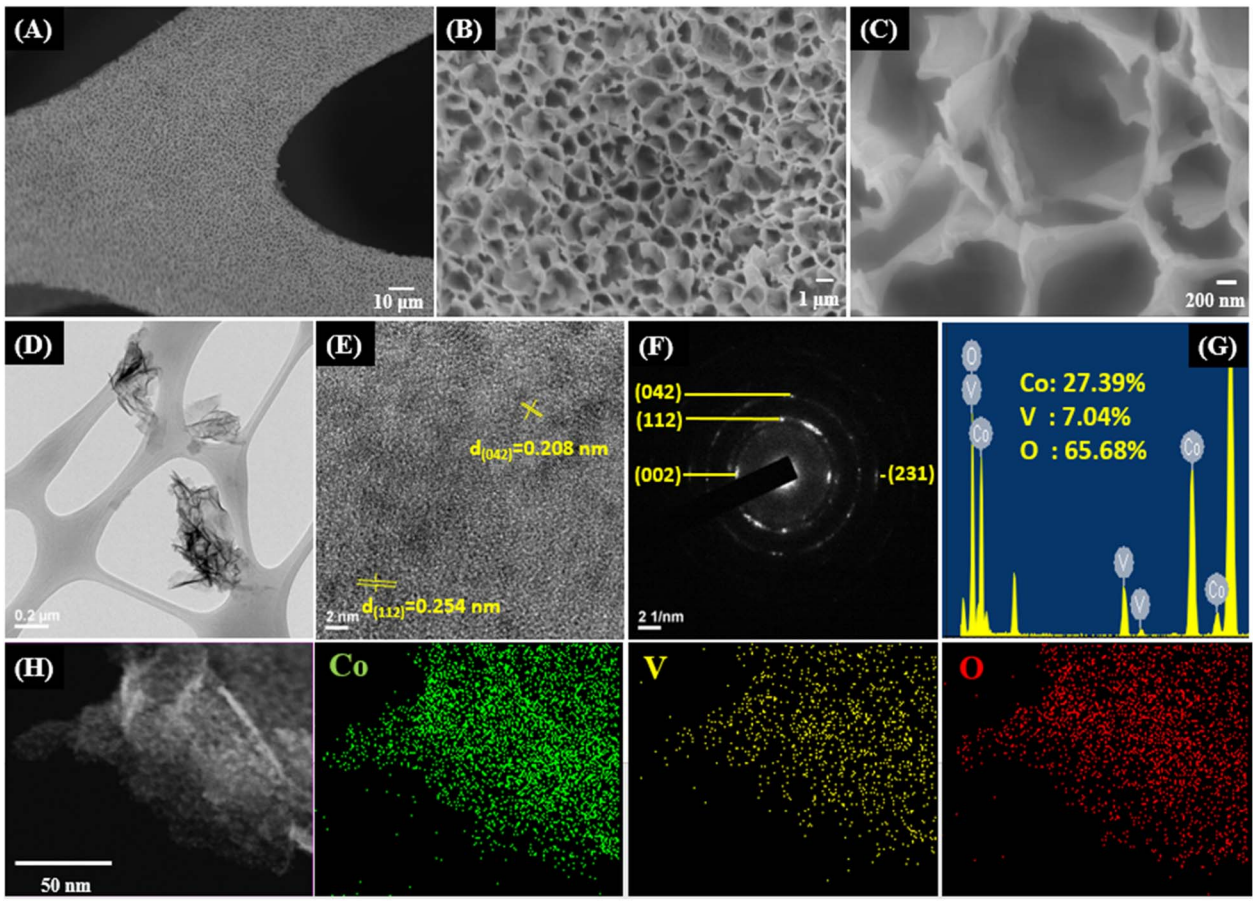

Fig. 1 (A–C) SEM images, (D–E) TEM images, (F) SAED pattern, (G) EDS elemental distribution, and (H) EDS mappings of O, V, and Co elements.

The Faraday reaction of $K_3Fe(CN)_6$ in RA electrolyte provides additional capacitance,[14] as shown in eqn (5) below.

$$Fe(CN)_6^{4-} \leftrightarrow Fe(CN)_6^{3-} + e^- \quad (5)$$

It is also seen that the RA electrolyte gives enhanced current densities, as seen in both of the redox pairs in Fig. 2B. In the first (left-hand side) redox peaks, the Co(II) ↔ Co(III) reaction is enhanced. This is attributed to the improvement of electrolyte conductivity by adding RA, which will be shown later.[28,29] For the second redox peaks, the enhancement is primarily due to the redox reactions of $K_3Fe(CN)_6$. This then leads to enhanced C_{sp}. The redox reaction occurring in the RA electrolyte is explained as followed.[23,30] During the charging process, the oxidation of Co occurs: Co^{2+} to Co^{3+} and Co^{3+} to Co^{4+}, leading to the loss of electrons. The electrons then transfer to $Fe(CN)_6^{3-}$ which then reduces to $Fe(CN)_6^{4-}$. The reversed process takes place during the discharge process. GCD curves obtained at various current densities using the KOH and RA electrolytes are shown in Fig.s S4B† and 2C, respectively. Longer discharge time is seen in the GCD curves obtained using the RA electrolyte, indicating improved C_{sp}. Both KOH and RA electrolytes exhibit pseudo-capacitive behaviors. The GCD curves obtained using the KOH show a plateau at about 0.05 V for Co(II) ↔ Co(III) and 0.29 V for Co(III) ↔ Co(IV).[18,31] In the case of the RA electrolyte, the lower plateau is insignificance. However the upper plateau is raised to a high V near 0.35 V, indicating the contribution of the redox-active $K_3[Fe(CN)_6]$.[28,29] The C_{sp} measured in different electrolytes was calculated using the GCD results (Fig. 2D). C_{sp} value of 109.9 mA h g^{-1} (878.9 F g^{-1}) at 1 A g^{-1} and rate retention of 58% (63.9 mA h g^{-1} (511 F g^{-1}) at 10 A g^{-1}) were obtained in the KOH electrolyte. Nearly two-fold improvement of the C_{sp} is seen when the RA electrolyte is used, giving a C_{sp} of 198.1 mA h g^{-1} (1584.5 F g^{-1}) at 1 A g^{-1} and the remaining 57% at 10 A g^{-1}.

The charge storage mechanism for $Co_3V_2O_8$ in KOH and RA electrolytes was analyzed using the following power law equation.[32,33]

$$i = av^b \quad (6)$$

where a, and b are constants, v is the scan rate from CV measurement, and i is the current. The value of b is used to determine if the charge storage is diffusion-controlled or surface-controlled as follows. For surface-controlled and diffusion-controlled charge storages, the values of b are 1 and 0.5, respectively.[34] As shown in Fig. 2E, the calculated values of b are 0.66 and 0.51 for the electrode measured in KOH and RA electrolytes, respectively. This indicates that the RA provides more diffusion-controlled charge storage, representing more

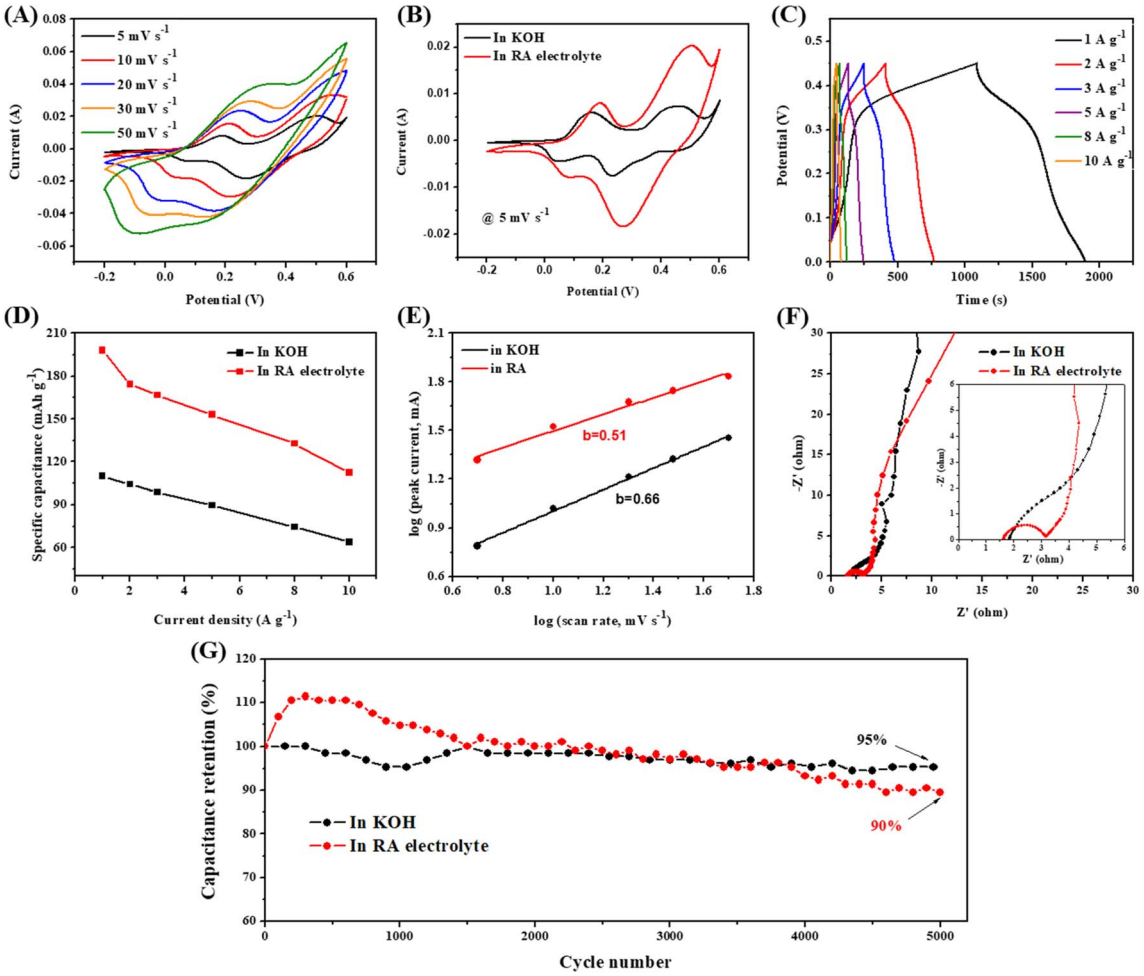

Fig. 2 (A) CV curves obtained using RA electrolyte. (B) Comparative CV curve of the sample tested in KOH and without RA electrolytes at 5 mV s^{-1}. (C) GCD curves collected using RA electrolyte at different current densities. (D) C_{sp} calculated based on the GCD curves. (E) Relationship between cathodic peak current with scan rates on KOH and RA electrolytes. (F) Nyquist plots and (G) Cycle performances obtained using the two different electrolytes.

Faradaic redox reactions occurring due to the use of RA electrolyte. The additional redox reactions are ascribed to the $Fe(CN)_6^{3-}/Fe(CN)_6^{4-}$ oxidation/reduction reactions, which are shown in the CV (Fig. 2B) and GCD (Fig. 2C) curves. Thus, the significant improvement in capacitance is obtained.

EIS investigation was done and is presented in Fig. 2F. The intercept between the curve and the *x*-axis represents the solution/electrolyte resistance (R_s), which is associated with the electrolyte ionic conductivity. Charge transfer resistance (R_{ct}) is depicted by the semicircle at high frequencies. The slope at the high-frequency region represents the electrolyte diffusion resistance (R_d).[23] The Nyquist plots exhibit that the R_s of RA electrolyte (1.6 Ω) is slightly lower than the value in KOH electrolyte (1.8 Ω). This indicates the better ionic conductivity in the RA electrolyte, which facilitates the ion movement to diffuse to the pores of the electrode. Furthermore, the R_{ct} value of $Co_3V_2O_8$ measured using the RA electrolyte is 1.5 Ω, which is lower than that of measured using 3 M KOH (3.2 Ω). The result indicates the faster electron transfer at the electrode/electrolyte interface in RA electrolyte and among the particle in the bulk electrode, which is beneficial for fast redox reactions. For the R_d, it is seen that the RA electrolyte smaller slope, indicating better ions diffusion into the pores of $Co_3V_2O_8$. These reduced resistances contribute to the improvement of the electrochemical performance. Cycling performances were examined *via* GCD measurement at a current density of 5 A g^{-1} for 5000 cycles in the KOH and 0.05 M $K_3[Fe(CN)_6]$ RA electrolytes, as shown in Fig. 2G. SEM images of the material after the cyclic testis in both electrolytes are presented in Fig. S5.† The $Co_3V_2O_8$ shows excellent cycle stability in both the KOH and RA electrolytes. However, the use of RA electrolyte shows lower stability than the use of KOH electrolyte. This is attributed to the crystallization of $K_3[Fe(CN)_6]$ and the aggregation of free ions during the prolonged $Fe(CN)_6^{3-}/Fe(CN)_6^{4-}$ redox process.[35,36] In addition, the redox additive involves intensive redox reactions at the interface of active electrode material and electrolyte, which promotes the rate of dissolution of active electrode material, leading to the cyclic retention degradation.[36]

To evaluate the material for practical application, ASC was assembled and tested. The CV curves of the AC negative

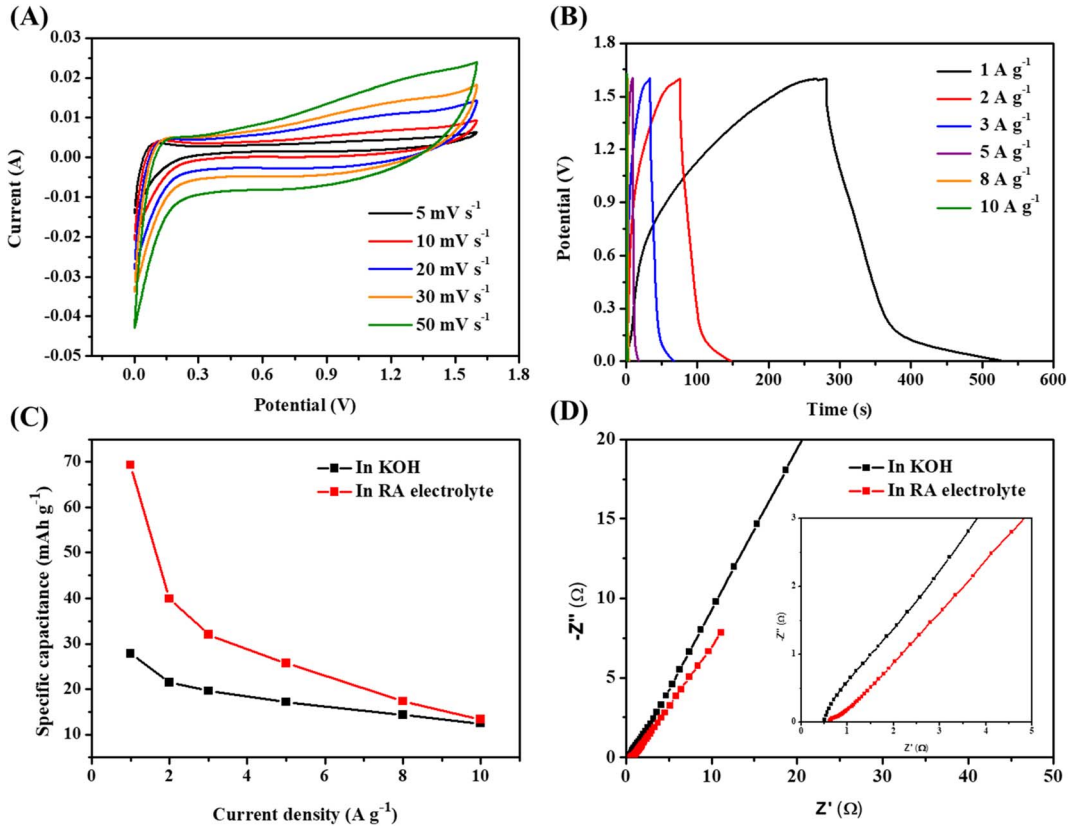

Fig. 3 (A) CV curves at various scan rates, (B) GCD curves at various current densities of $Co_3V_2O_8$//AC ASC in RA electrolyte. (C) C_{sp} of the two ASC calculated from GCD curves. (D) Nyquist plots of the ASCs obtained using KOH and RA electrolytes.

electrode are displayed in Fig. S6A,† which shows no redox peak. The GCD curves show typical electrical double layer capacitor behavior of carbon (Fig. S6B†). The C_{sp} is 38.8 mA h g^{-1} (139 F g^{-1}) at 1 A g^{-1} (Fig. S6C†). Fig. S7A† shows the CV curves of the positive and negative electrodes at 5 mV s^{-1} in 3 M KOH. Fig. S7B† shows that the optimized cell voltage is 1.6 V. The CV curves of the ASC in KOH electrolyte with a cell voltage of 1.6 V is shown in Fig. S8A.† The CV curves of ASC obtained using the RA electrolyte are presented in Fig. 3A. All CV curves exhibit pseudocapacitive behavior. A higher current response is seen in the CV curves of the ASC having RA electrolyte, demonstrating the superior electrochemical performance. Fig. 3B and S8B† presented the GCD curves of the ASCs in the RA and KOH electrolytes, respectively. The discharge time of the ASC using the RA electrolyte is longer than that of the ASC using the KOH electrolyte, indicating higher capacitance in the former. Fig. 3C shows the C_{sp} derived from the GCD curves of the two ASCs. In comparison, the C_{sp} of the ASC utilizing RA

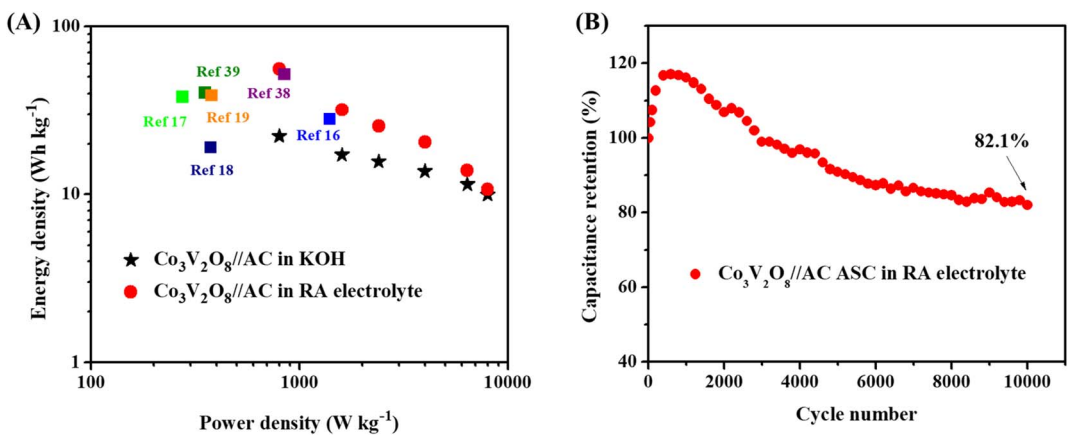

Fig. 4 (A) Ragone plot correlating E_d and P_d and (B) Cyclic stability of $Co_3V_2O_8$//AC ASC devices using KOH and RA electrolytes.

electrolyte is 69.3 mA h g^{-1} (156 F g^{-1}), more than two times higher than the ASC using KOH electrolyte (27.8 mA h g^{-1} (63 F g^{-1})). Fig. 3D show the Nyquist plots of the two ASCs. In comparison to the ASC using the 3 M KOH electrolyte (R_{ct} = 1.52 Ω), the ASC using the RA electrolyte exhibits a reduced R_{ct} of 0.32 Ω. This indicates better charge transfer in the RA electrolyte, contributing to the improvement of the C_{sp}.[37] Also, the ASC with the RA electrolyte gives a high E_d of 55.5 W h kg^{-1} at a high P_d of 800 W kg^{-1}, as shown in Fig. 4A. For comparison, the ASC using the 3 M KOH delivers an E_d of 22.2 W h kg^{-1} at the same P_d. It is noted that the obtained E_d in this work outperforms most previously reported cobalt vanadate-based materials, such as $Co_{1.5}Ni_{1.5}V_2O_8$//AC (51.6 W h kg^{-1} at 850 W kg^{-1}),[38] $Co_2V_2O_7$//rGO (19 W h kg^{-1} at 375.8 W kg^{-1}),[18] Ni_2P–$Co_3V_2O_8$//AC (40.2 W h kg^{-1} at 353 W kg^{-1}),[39] Co_3O_4–$Co_3V_2O_8$//AC (38 W h kg^{-1} at 275 W kg^{-1}),[17] $Ni_3V_2O_8$/$Co_3V_2O_8$//AC (28 W h kg^{-1} at 1400 W kg^{-1}),[16] and NiO–$Co_3V_2O_8$//AC (38.8 W h kg^{-1} at 379.7 W kg^{-1}).[19] The cycle stability of the ASC in 0.05 M $K_3[Fe(CN)_6]$ RA electrolyte was determined *via* GCD measurement at a current density of 5 A g^{-1}. As shown in Fig. 4B, the ASC exhibits 82.1% capacitance retention after 10 000 cycles. The reduction of capacitance is due to the occurrence side-reactions and the decreased activity of the redox additive during the long GCD measurement time.[35,40,41]

4. Conclusion

We report cobalt vanadate nanowalls grown on nickel foam for use as an electrode of supercapacitors. The nanostructured $Co_3V_2O_8$ demonstrates a high specific capacitance of 109.9 mA h g^{-1} (878.9 F g^{-1}) at 1 A g^{-1} in KOH. The use of $K_3Fe(CN)_6$ redox additive further improves the electrochemical performance, giving nearly two-time enhancement of the capacitance (198.9 mA h g^{-1} (1584.5 F g^{-1})). ASC consisting of $Co_3V_2O_8$ positive electrode, AC negative electrode, and redox additive electrolyte delivers a high energy density of 55.5 W h kg^{-1} at a power density of 800 W kg^{-1} and good cyclic stability. The excellent electrochemical performance shows that the $Co_3V_2O_8$ is an excellent electrode material for the next-generation supercapacitor.

Conflicts of interest

The authors declare that there is no competing financial interest that could have appeared to influence the work reported in this paper.

Acknowledgements

The study was supported by the Ministry of Science and Technology, Taiwan through grant no. MOST 110-2221-E-006-115 and the Hierarchical Green-Energy Materials (Hi-GEM) Research Center, from The Featured Areas Research Center Program within the framework of the Higher Education Sprout Project by the Ministry of Education and the Ministry of Science and Technology (MOST 111-2634-F-006-008) in Taiwan.

References

1 R. Chen, P. Shi, Y. Gong, C. Yu, L. Hua, L. Li, J. Zhou, T. Xu, Y. Zhang and G. Sun, *Energy Technol.*, 2018, **6**, 2326–2332.
2 R. Chen, J. Xue, X. Gao, C. Yu, Q. Chen, J. Zhou, G. Sun and W. Huang, *Nanoscale*, 2020, **12**, 22075–22081.
3 H. Xu, X. Zhao, C. Yu, Y. Sun, Z. Hui, R. Zhou, J. Xue, H. Dai, Y. Zhao and L. Wang, *Nanoscale*, 2020, **12**, 11112–11118.
4 G. R. Wang, Z. L. Jin and W. X. Zhang, *Dalton Trans.*, 2019, **48**, 14853–14863.
5 S. Sheng, W. Liu, K. Zhu, K. Cheng, K. Ye, G. L. Wang, D. X. Cao and J. Yan, *J. Colloid Interface Sci.*, 2019, **536**, 235–244.
6 M. Khalid, P. Bhardwaj and H. Varela, in *Science, Technology and Advanced Application of Supercapacitors*, IntechOpen, 2018.
7 L. Hua, P. Shi, L. Li, C. Yu, R. Chen, Y. Gong, Z. Du, J. Zhou, H. Zhang and X. Tang, *ACS Appl. Mater. Interfaces*, 2017, **9**, 37022–37030.
8 X. Lv, W. Huang, Q. Shi, L. Tang and J. Tang, *J. Power Sources*, 2021, **492**, 229623.
9 J. Acharya, T. H. Ko, M.-K. Seo, M.-S. Khil, H.-Y. Kim and B.-S. Kim, *ACS Appl. Energy Mater.*, 2020, **3**, 7383–7396.
10 L. Li, R. Chen, Y. Gong, C. Yu, Z. Hui, H. Xu, X. Zhao, Y. Sun, W. Zhao and G. Sun, *J. Mater. Chem. A*, 2019, **7**, 107–111.
11 Y. Gong, J. An, H. Dai, R. Chen, C. Yu, Q. Chen, J. Zhou, G. Sun and W. Huang, *Electrochim. Acta*, 2020, **356**, 136843.
12 Y. Teng, Y. Li, D. Yu, Y. n. Meng, Y. Wu, X. Zhao and X. Liu, *ChemistrySelect*, 2019, **4**, 956–962.
13 W. H. Low, C. W. Siong, C. H. Chia, S. S. Lim and P. S. Khiew, *J. Sci.: Adv. Mater. Devices*, 2019, **4**, 515–523.
14 Z. Khan, B. Senthilkumar, S. Lim, R. Shanker, Y. Kim and H. Ko, *Adv. Mater. Interfaces*, 2017, **4**, 1700059.
15 H. Hosseini and S. Shahrokhian, *Chem. Eng. J.*, 2018, **341**, 10–26.
16 M.-C. Liu, L.-B. Kong, L. Kang, X. Li, F. C. Walsh, M. Xing, C. Lu, X.-J. Ma and Y.-C. Luo, *J. Mater. Chem. A*, 2014, **2**, 4919–4926.
17 W.-B. Zhang, L.-B. Kong, X.-J. Ma, Y.-C. Luo and L. Kang, *J. Power Sources*, 2014, **269**, 61–68.
18 H. Sun, X. Chen, H. Chai, Y. Wang, D. Jia, Y. Cao and A. Liu, *Appl. Surf. Sci.*, 2019, **469**, 118–124.
19 W.-B. Zhang, L.-B. Kong, X.-J. Ma, Y.-C. Luo and L. Kang, *J. Alloys Compd.*, 2015, **627**, 313–319.
20 H. Hosseini and S. Shahrokhian, *Chem. Eng. J.*, 2018, **341**, 10–26.
21 A. Akram, M. A. Liaqat, S. Javed, M. Hamid, U. Ali, F. Javed, M. Wei and M. A. Akram, *J. Alloys Compd.*, 2022, **891**, 161961.
22 P. Samanta, S. Ghosh, N. C. Murmu and T. Kuila, *Composites, Part B*, 2021, **215**, 108755.
23 Y. Zhao, J. Zheng, M. Yuan, Y. Wang, W. Liu, S. Yang, G. Li, J. Lian and Y. Bu, *J. Alloys Compd.*, 2021, **885**, 160886.
24 G. Dhakal, D. Mohapatra, T. L. Tamang, M. Lee, Y. R. Lee and J.-J. Shim, *Energy*, 2020, 119436.
25 D. B. Bailmare, P. Tripathi, A. D. Deshmukh and B. K. Gupta, *Sci. Rep.*, 2022, **12**, 1–10.

26 Y. Li, L. Kong, M. Liu, W. Zhang and L. Kang, *J. Energy Chem.*, 2017, **26**, 494–500.
27 T. Zhai, L. Wan, S. Sun, Q. Chen, J. Sun, Q. Xia and H. Xia, *Adv. Mater.*, 2017, **29**, 1604167.
28 Y. Chen, J. Huang, X. Zhang and H. Xu, *J. Electroanal. Chem.*, 2021, **884**, 115069.
29 C. Zhao, W. Zheng, X. Wang, H. Zhang, X. Cui and H. Wang, *Sci. Rep.*, 2013, **3**, 2986.
30 L.-H. Su, X.-G. Zhang, C.-H. Mi, B. Gao and Y. Liu, *Phys. Chem. Chem. Phys.*, 2009, **11**, 2195–2202.
31 M. Amiri, S. S. H. Davarani, S. K. Kaverlavani, S. E. Moosavifard and M. Shamsipur, *Appl. Surf. Sci.*, 2020, **527**, 146855.
32 J. Pokharel, A. Gurung, A. Baniya, W. He, K. Chen, R. Pathak, B. S. Lamsal, N. Ghimire and Y. Zhou, *Electrochim. Acta*, 2021, **394**, 139058.
33 R. Mohanty, G. Swain, K. Parida and K. Parida, *J. Alloys Compd.*, 2022, 165753.
34 V. T. Nguyen and J.-M. Ting, *ACS Sustainable Chem. Eng.*, 2020, **8**, 18023–18033.
35 P. Samanta, S. Ghosh, N. C. Murmu and T. Kuila, *Composites, Part B*, 2021, **215**, 108755.
36 N. R. Chodankar, D. P. Dubal, A. C. Lokhande, A. M. Patil, J. H. Kim and C. D. Lokhande, *Sci. Rep.*, 2016, **6**, 1–14.
37 J. Fu, L. Li, D. Lee, J. M. Yun, B. K. Ryu and K. H. Kim, *Appl. Surf. Sci.*, 2020, **504**, 144250.
38 B. Huang, W. Wang, T. Pu, J. Li, C. Zhao, L. Xie and L. Chen, *Chem. Eng. J.*, 2019, **375**, 121969.
39 Y.-M. Hu, M.-C. Liu, Y.-X. Hu, Q.-Q. Yang, L.-B. Kong, W. Han, J.-J. Li and L. Kang, *Electrochim. Acta*, 2016, **190**, 1041–1049.
40 M. He, K. Fic, E. Fra, P. Novák and E. J. Berg, *Energy Environ. Sci.*, 2016, **9**, 623–633.
41 X. Liu, Z. Lu, H. Pan, J. Cheng, J. Dou, X. Huang and X. Chen, *Electrochim. Acta*, 2022, **429**, 141056.